J Electroceram (2011) 26:175–184
DOI 10.1007/s10832-011-9642-y

Analytical model and optimal design of a d_{33}-mode active layer for the lightweight unimorph piezo-composite actuator

Ngoc-Trung Nguyen · Bum-Soo Yoon · Ki-Hoon Park · Kwang-Joon Yoon

Received: 9 December 2009 / Accepted: 29 May 2011 / Published online: 6 May 2011

Abstract This paper presents an analytical model, simulation and optimal design of a d_{33}-mode lightweight piezo-composite unimorph actuator (d_{33}-mode LIPCA). The actuator consists of a PZT layer bonded to several other composite prepreg layers. In which, the interdigitated electrodes (IDE) are deposited on the surfaces of the PZT material. The PZT layer is poled in-plane and operated in the semi d_{33}-mode. Since the d_{33} coefficient is normally twice of d_{31} value, the actuation performance of d_{33}-mode LIPCA is expected to be improved significantly. Performance predictions of the d_{33}-mode LIPCA are done by using the finite element method with a coupled-field model. Design of the IDE system patterned on the PZT surfaces is optimized in a poling process analysis to achieve the highest portion of PZT material poled in the longitudinal direction. Effect of the design variables such as electrode width, gap between electrodes and applied voltage for poling process is also performed numerically.

Keyword LIPCA · d_{33}-mode · Piezo-composite actuator · Interdigitated electrodes

1 Introduction

During the past decade, many investigations have been conducted on application of smart materials to build effective and compact actuators. Several small, powerful, and reliable actuators using piezoelectric ceramic materials have been invented, e.g. AFC™ (MIT), THUNDER™ and LaRC-MFC™ (NASA Langley Research Center) [1, 2]. Among them, LIPCA (**LI**ghtweight **P**iezo-**C**omposite **A**ctuator) was introduced as one of the excellent unimorph actuator suitable for wide range of applications [3–5]. LIPCA is designed to operate with d_{31} actuation mechanism by utilizing the excitation in transverse direction. To fabricate LIPCA, a glass/epoxy fabric prepreg is placed as the bottom layer on a flat base plate and a PZT ceramic wafer with silver pasted copper strip wires are placed on the glass/epoxy prepreg. A carbon/epoxy unidirectional prepreg and glass/epoxy fabric prepreg is stacked over the ceramic wafer in accordance with the lay-up design. The stacked layers are then vacuum bagged and cured at an elevated temperature (177°C) following an autoclave bagging process. LIPCA has lighter weight than any other piezo-actuator thus it is most suitable as artificial muscle for biomimetic robots [6–8]. Although LIPCA shows its advantages in application to bio-robot field, the actuation it generates is still small. Demand on improving the performance of actuators is thus obvious. Recently, in experimental studies [9–11], the authors showed that with a preferable arrangement and loading, LIPCA could give higher actuation displacement values. In an application of the flapping device [7], the compressive LIPCA has also been proven to improve 22% in flapping angle and lifting force compared to that of the original LIPCA without compression at 300 V_{pp} (applied peak-to-peak voltage). Another approach to improve the performance of LIPCA is applying the direct piezoelectric effect along the poling

N.-T. Nguyen · B.-S. Yoon · K.-H. Park · K.-J. Yoon (✉)
Department of Aerospace Information System Engineering,
Konkuk University,
Seoul 143-701, South Korea
e-mail: kjyoon@konkuk.ac.kr

direction (using d_{33}-mode actuation) instead of using transverse direction (d_{31}-mode actuation) where the piezoelectric coefficient d_{33} is almost twice larger than the d_{31} value [6, 12]. The induced strain of PZT layer with d_{33} actuation mechanism is thus higher than that with d_{31} actuation mechanism. Some research papers can be listed here as attempts to use d_{33} actuation mechanism in actuator. Yoon et al. [13] have proposed an idea of the stacked ceramic thin embedded **I**nter**D**igitated **E**lectrode **A**ctuation **L**ayer (IDEAL). The AFC™ (MIT) and LaRC-MFC™ (NASA Langley Research Center) also used d_{33} actuation for piezoceramic fiber with surface interdigitated electrodes (IDEs) to improve the actuation performance [1, 14]. However, fabrication of these d_{33}-mode actuators is somehow complicated and costly. Moreover, the attenuation of the driving electric fields phenomenon occurring in the AFC™/MFC™ actuators due to the unwanted accumulations of epoxy between the electrodes and the ceramics is still an unsolved issue [2, 15].

This research aims to achieve an improvement of actuation performance for LIPCA by introducing the concept of a d_{33}-mode active layer as well as making use of the enhancement of PZT performance under residual compressive stress due to curing process. This d_{33}-mode LIPCA has an interdigitated electrode (IDE) system patterned on surfaces of a bulk PZT wafer to make a d_{33}-mode actuation layer. The ceramic layer is stacked with other constituent material layers in accordance with an appropriate lay-up design to form a unimorph actuator similar as in the case of LIPCA shown in Fig. 1. The d_{33}-mode LIPCA requires a poling process by applying high voltage through IDEs to achieve the desired in-plane poling status. A comparison with the regular LIPCA by using an analytical model shows that the performance of the new design can be improved considerably. Numerical simulation also shows that the optimal active layer with d_{33}-mode operation can generate much higher strain compared to that in d_{31}-mode.

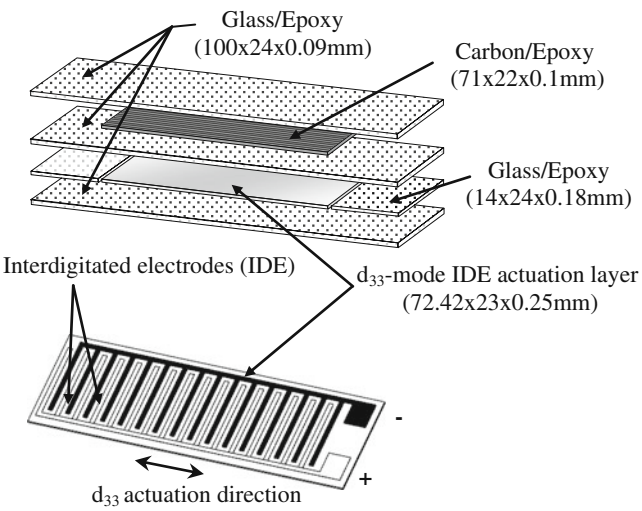

Fig. 1 Layup structure of the d_{33}-mode LIPCA

Previously, only a few studies on optimization of the IDE system design have been published [16, 17]. However, most of the authors focused on the excitation condition. They somehow assumed that the material was uniformly poled in the longitudinal direction and then tried to maximize the strain. Yet the design of a IDE system patterned on the PZT surfaces strongly affects the overall performance of the d_{33}-mode LIPCA. The electrode spacing and electrode width determine the distribution, direction and concentration of the electric field in PZT in both cases: poling process and operating condition. Electric field distribution and intensity are extremely important in poling process which establishes the behavior of the active layer later on. Those two design parameters together with the applied poling voltage determine how many percentage of the ceramic material will contribute to the actuation in d_{33} mode and also limit the highly concentrated electric field zone to avoid potential failure. The design of the surface IDE system should be optimized.

2 Design of the piezo-composite actuator LIPCA

LIPCA is designed to have large actuating moment by increasing the distance from the flexural neutral surface of the actuator to the center of the actuating layer. A glass/epoxy layer with the full length of the actuator is imbedded between the ceramic wafer and the carbon/epoxy layer to increase the moment arm distance and to prevent a crack initiation problem at the edges of ceramic wafer. Another layer of glass/epoxy was placed on the top surface of the carbon/epoxy layer to protect the PZT ceramic wafer from external impact and for the electrical insulation of the carbon/epoxy top layer. The material and physical properties of each layer are given in Table 1. The stacked layers are then vacuum bagged and cured at an elevated temperature (177°C) following an autoclave bagging process. Mismatching in coefficient of thermal expansion (CTE) of constituent materials leads to the curved shape of manufactured actuators and induced stress in each layer. To compare the actuating performance between the original LIPCA (d_{31}-mode) and the improved one (d_{33}-mode), the lay-up design, materials, and all dimensions are kept unchanged in this study. The PZT wafer is of 72.42 mm length, 23 mm width and 0.25 mm thickness. The difference between two actuators is thus only the actuation mechanism of the electro active layer.

The actuation displacement of a unimorph actuator is produced by the curvature change of the laminated structure

Table 1 Properties of constituent materials of LIPCA (after [5])

Properties		PZT	Carbon/Epoxy	Glass/Epoxy
Modulus	E_1 (GPa)	62	231.2	21.7
	E_2 (GPa)	62	7.2	21.7
	E_3 (GPa)	49	7.2	0.217
	G_{12} (GPa)	23.66	4.3	3.99
	ν_{12}	0.31	0.29	0.13
Piezoelectric strain coefficient	d_{31} $(\times 10^{-12} m/V)$	−320	–	–
	$d_{33}(\times 10^{-12} m/V)$	650	–	–
CTE	α_1 $(10^{-6} K^{-1})$	3.5	−1.58	14.2
	α_2 $(10^{-6} K^{-1})$	3.5	32.2	14.2
Product/Manufacturer		3203HD, CTS	UPN-116B, SK Chemicals	GEP-108, SK Chemicals

when an electric field is applied on an electro active layer [5]. The actuating mechanism of a multi-layered beam structure can be described as in Fig. 2.

In Fig. 2, a is the moment arm, ΔP_a represents the change in the actuating force of the electro active layer generated due to the change in the electric field, and ΔM_a represents the change in the bending moment. For an actuator beam with unit width, the change in the curvature can be expressed as follows:

$$\Delta\kappa = \frac{1}{\Delta\rho} = \frac{\Delta M_a}{D} \tag{1}$$

where $D = \sum E_i I_i$ is the total bending stiffness which is the sum of the bending stiffness of each layer with respect to the neutral axis, E_i and I_i are the modulus and the area moment of inertia of each layer. The change in the actuation moment ΔM_a is the vector product of the actuation force change ΔP_a and the moment arm a. The change in the actuation force ΔP_a can be obtained from the multiplication of the area of actuation layer cross section $A_a(= 1 \times t_a)$ per unit width, the elastic modulus of PZT layer E_a, and the strain $d_{ij} \times \Delta E$ induced from the change in the electric field

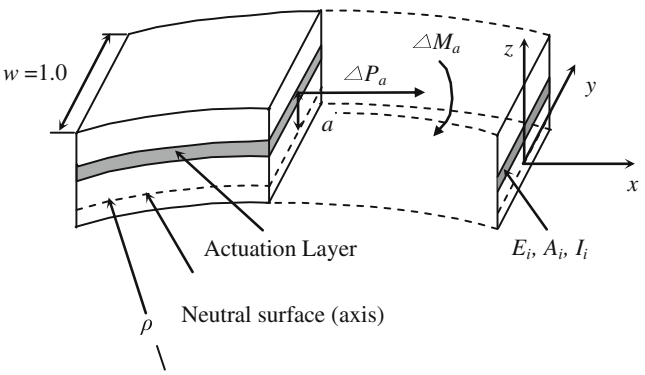

Fig. 2 Curvature change of a laminated beam with electro active layer [5]

where d_{ij} is the electro-active strain coefficient, ΔE is the electric field change. Therefore, ΔM_a can be expressed as:

$$\Delta M_a = a \times t_a \times E_a \times d_{ij} \times \Delta E \tag{2}$$

Then, the change in the curvature is:

$$\Delta\kappa = \frac{a}{D} \times t_a \times E_a \times d_{ij} \times \Delta E = c_{cua} \times \Delta E \tag{3}$$

where, the *curvature coefficient of a unimorph actuator* is defined by $c_{cua} = \frac{a}{D} t_a E_a d_{ij}$

It is clear that the moment arm length a from the flexural neutral surface of the actuator beam to the center of the actuating layer must be as large as possible to have a larger actuating moment, which means that the actuating layer should be placed on one of the outer surfaces. In addition, the total bending stiffness of an actuator section should be small to have a large curvature change for a given actuation moment. Thus, the larger value c_{cua} is, the higher actuation displacement can be achieved. With the given geometry (Fig. 1) and properties of constituent materials (Table 1) of LIPCA we have a comparison for LIPCA operated with d_{31}-mode and with d_{33}-mode as shown in Table 2. It should be noted here that the geometry and lay-up structure in two cases are identical. The only difference is the actuation mechanism of the active layer.

For the same given values of the PZT thickness t_a and the applied electric field change ΔE, LIPCA operating with d_{33}-mode can theoretically generate a curvature change almost twice of that in d_{31}-mode LIPCA case. However, to fabricate a fully d_{33}-mode actuator is not trivial. The d_{33}-mode LIPCA using surface interdigitated electrodes (IDEs) piezoelectric ceramic wafer as the actuation layer in this work is not a perfect d_{33}-mode actuation mechanism. The d_{33}-mode LIPCA requires a poling process which is realized by applying high voltage through IDEs to achieve the desired poling status. When an electrical input is applied using the IDE system, the in-plane electric fields

Table 2 Comparison of actuator performances and characteristics

Quantity	Symbol	Unit	d_{31}-mode	d_{33}-mode
Bending stiffness	D	$(\times 10^{-3}\ N{\cdot}m^2)$	24.1	22
Moment arm	a	(mm)	0.151	0.163
c_{cua}	$c_{cua} = \frac{a}{D} t_a E_a d_{ij}$	$(V^{-1}{\cdot}m^{-1})$	$0.123 t_a$	$0.236 t_a$
Actuation moment	ΔM_a	$(\times 10^{-3} N{\cdot}m)$	$3.0\ t_a \Delta E$	$5.2 t_a \Delta E$
Curvature change	$\Delta\kappa = \frac{\Delta M_a}{D}$	(m^{-1})	$0.124 t_a \Delta E$	$0.236 t_a \Delta E$

in ceramic are inhomogeneous. There exists '*dead zones*' where electric fields are low or in out-of-plane directions. Thus, the piezoelectric material is not actuated in a fully d_{33}-mode. An appropriate design of the surface IDE system that could improve much the performance of the piezoelectric material by approaching the perfect d_{33}-mode is the goal of this study.

3 Optimal design of the d_{33}-mode active layer

The piezoelectric effect, i.e., the electro-mechanical coupling, is not present in a virgin material but appears during the poling procedure when a certain electric field acts onto the material. In practice, the required field can only be applied after the manufacturing process through the surface IDEs configuration. Thus, the material has a locally inhomogeneous poling field distribution thereby inducing an inhomogeneous distribution of piezoelectric properties. However, research on poling and its contribution to the overall performance of actuators with surface IDEs system is limited [16, 17]. Works on the optimization problem of surface IDE d_{33}-mode actuators such as MFC and AFC design mostly focused on the actuating phase and assumed that the piezoelectric material is uniformly poled in the actuating direction [17, 18]. This assumption is not adequate since the poling of these actuators through surface IDEs system makes the electric field inhomogeneous and thus the polarization state in the material is strongly non-uniform, especially for the case of small gaps between two electrode lines [16]. Experimental study also showed that the performance of MFC is largely dependent on the configurations of the IDE system in poling tests [19]. The numerical analysis of the poling process for devices with surface IDEs system has been studied by the authors [20]. In which, poling is an incremental process where an electrical (voltage) loading is applied step by step. During the process, material properties of the actuator change with the poling state it obtains. The simulation in this case is thus an incremental loading and the material properties are updated after each loading step. From the poling analysis results, one will have a better understanding on the poling process for actuators with surface IDE systems, e.g. AFC and MFC, to build a guideline to obtain the optimum design for a IDE system in the sense of the level of poling state. To achieve the optimum design of the IDE actuation layer, an optimization analysis is performed using ANSYS® Multiphysics finite element package through an electromechanical coupled-field and linear analysis.

3.1 Finite element modeling of the poling process

The numerical analysis of the poling process for devices with surface IDEs system has been studied by the authors [20]. In this section we briefly outline some key points of the method. By ignoring the influence of edge effects at the physical ends, the actuation layer can be decomposed into repeating unit cells of identical behavior. A finite element model of the representative volume element (RVE) is built for the IDE actuation layer as shown in Fig. 3. Although the device is three-dimensional, the problem solving the electrical field can be simplified as a two-dimensional model because the electric field distribution does not vary along the width (z-direction). The 2D model can take the advantage of symmetry to

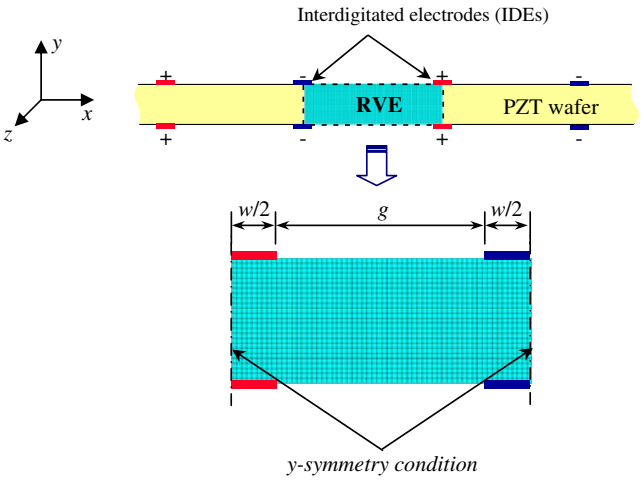

Fig. 3 Representative volume element of the surface IDE actuation layer (not to scale)

scale down the problem size and to lower the required computing resources and time as well. Computational benchmarks and tests have been conducted to claim that the field solution in 2D model is almost identical to that of the 3D model [20]. Since the repeating RVE has an identical electric field based on the geometry of the IDEs, the piezoelectricity of the whole active layer can be defined by determining the electromechanical properties of the unit cell.

The unpoled PZT ceramic wafer is assumed to be isotropic and to have the dielectric constant 60% that of the poled value [21]. The poled properties are given at CTS Corporation website (www.ctscorp.com). It is assumed that the electrodes do not contribute to the electrical and mechanical response of the active layer much and are not modeled explicitly in the model. The electrical signal (voltage) is thus applied directly on nodes located on the surface where electrodes are patterned. The *y*-symmetry boundary conditions are imposed on the two vertical sides of the RVE.

An evolutionary, incremental solution was employed to monitor the growth of poled region and the development of potential breakdown areas. The piezoelectricity coefficients are functions of the direction of polarization. The given values from the ceramics manufacturer can only be used for a fully poled material. In general case the coefficients are proportional to the remanent polarization. In FEM simulation, the updated piezoelectricity in each element is implemented by rotating the element coordinate system according to the direction of polarization within that element. By imposing the voltage incrementally through the IDEs, the local electric field value in material increases. To determine the poling state in an element, the poling strength at the integration point is defined on the basis of electric field distribution [16]:

$$X = 0 \text{ if } |E| < E_C; \tag{4}$$

$$X = \frac{E - E_C}{E_S - E_C} \text{ if } E_C < |E| < E_S;$$

$$\text{and } X = 0 \text{ if } |E| \geq E_C$$

where E_C and E_S are the *coercive field* and *saturation field* values respectively. As a rule of thumb, the *saturation field* value is approximately double the *coercive field* value [21]. Table 3 gives typical property values of CTS 3203HD PZT.

When the local electric field E approaches the *coercive value* E_C, domain switching occurs and the polarization aligns to the electric field vector direction. The material becomes partially poled. The local properties of partially poled regions can be simply determined as a function of the poling strength by [16]:

Table 3 Typical property values of PZT material (*source*: CTS Corp.)

Properties		CTS 3203HD
Dielectric constant	K_3^T	3800
Coercive field	E_C (kV/mm)	0.8
Remanent polarization	P^R $(\mu C/cm^2)$	39
Elastic constants (short circuit)	S_{11}^E $(\times 10^{-12}\ m^2/N)$	16.6
	S_{33}^E $(\times 10^{-12} m^2/N)$	21
	ν_{12}	0.31
Piezoelectric strain coefficient	d_{31} $(\times 10^{-12} m/V)$	−320
	d_{33} $(\times 10^{-12} m/V)$	650

$$c_{ij}^E = \left(c_{ij}^{E,fp} - c_{ij}^{E,up}\right)X + c_{ij}^{E,up}; \tag{5}$$

$$\varepsilon_l^T = \left(\varepsilon_l^{T,fp} - \varepsilon_l^{T,up}\right)X + \varepsilon_l^{T,up};$$

$$\text{and } d_{li} = d_{li}^{fp} X$$

where $c_{ij}^{E,up}, \varepsilon_l^{T,up}$ are the unpoled stiffness and dielectric constants; $c_{ij}^{E,fp}, \varepsilon_l^{T,fp}, d_{li}^{fp}$ are the fully poled stiffness, dielectric and piezoelectric constants, respectively. The actuator was assumed to be poled gradually with the increasing electric field after exceeding the *coercive field* value. When the local electric field reaches the *saturation field* value, the material becomes fully poled. The piezoelectric coefficients given by the manufacturer can be applied with the polarization direction coincides that of the local electric field. During the poling process, only the material portions with the value of the electric field lager than the *saturation value* will be fully poled.

In each incremental step, a loop is triggered to update of the material properties according to the poling strength, to re-calculate the electric field solution and to compare that with the former solution of each element. The iteration stops when a predefined criterion on the difference in orientation and magnitude of the electric field is reached. The poling process simulation was implemented in the ANSYS Parametric Design Language (APDL) using the advanced techniques to access the electric field solutions of the integration point in every element at the end of each iteration to check the poling status and update the material properties. The procedure can be summarized in Chart 1.

Simulation of the poling process for IDE ceramic wafer is shown in Fig. 4. A typical result reveals that the electric field distribution in RVE is strongly inhomogeneous and anisotropic. There are different regions:

- *Effective region* (A): the electric field is homogeneous; material is polarized along the longitudinal axis.

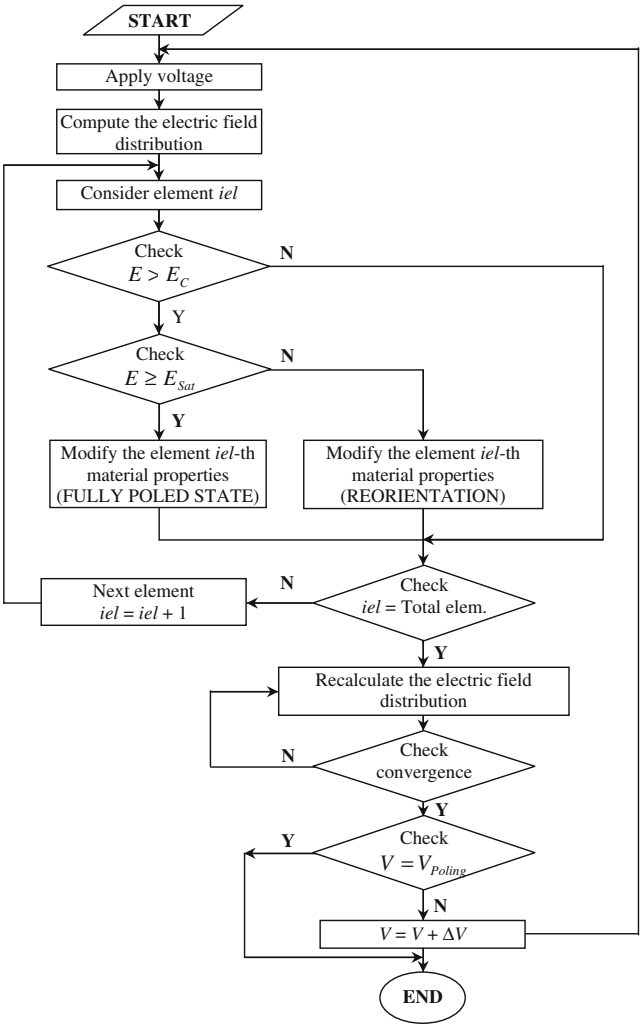

Chart 1 Flow chart for the simulation of poling process

- *Transition region* (B): high field concentration occurs here, this is the source of potential failure, and the contribution to actuation is small.
- *Ineffective region* (C + D): low electric field (C) or the field direction diverts from 3-direction (D); material is thus unpoled (C) or poled in vertical direction (D).

A perfect d_{33}-mode actuation is not achieved in this case. As shown in Fig. 4, only region A could contribute to the actuation along the longitudinal direction (perfect d_{33}-mode). The other regions (B, C and D) are considered as reduction of actuation compared to the fully d_{33}-mode. A good design should give a dominant region A over the whole volume.

3.2 Optimal design analysis

Based on the obtained electric field, piezoelectricity of the PZT wafer is defined. Actually, poling is an incremental process where electrical loading (voltage) is applied step by step. During the process, material properties of the actuator are updated with the poling state it obtains. The simulation in this case is thus an incremental loading with modification of material properties after each loading iteration [20]. In more complex case, with the presence of mechanical stress, the poling state depends on the switching phenomenon of domains under electromechanical loading. The poling process should be considered with an associated criterion for domain switching [22–24].

The design objective of the active layer is obtaining the highest fraction of PZT wafer poled in longitudinal direction and also satisfying a constraint on the highest field value to be smaller than a *breakdown value* to avoid potential failure of material. To achieve the optimum design of the IDE actuation layer, an optimization analysis is performed using ANSYS® Multiphysics finite element package with capability of electromechanical coupled-field and linear analysis. The goal of this study is to maximize the longitudinally poled portion (region A) and, at the same time, to minimize the high field zone (region B). A method of weighted combination for multi-objective optimization has been used to express the unequal contribution of each design objective in the total objective function [20, 25].

The principal design variables are chosen as the PZT thickness (t), the electrode width (w) and the gap between electrodes (g) as shown in Fig. 5. Range of value for each variable is constrained by the capability of fabrication and the operating conditions. For comparing purpose, the thickness of the PZT wafer is chosen the same as in the original LIPCA; that is 250 μm. Another study on the optimum thickness of PZT layer will be presented in a separated paper. Previous studies [16, 17] have shown that the larger gap between electrodes, the higher strain can be generated. However, with a large gap, the operating voltage will be increased. That could be an inconvenience for biomimetic robots application which requires a light weight on-board power source to be autonomous. The gap is then

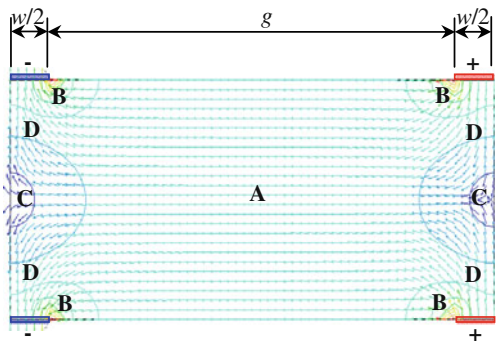

Fig. 4 Electric field distribution in the RVE

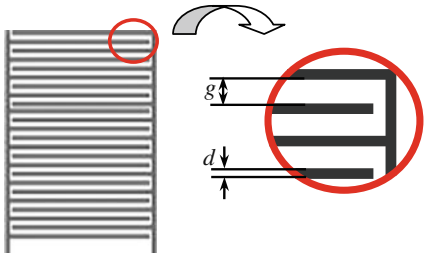

Fig. 5 PZT with electrodes patterned on surfaces

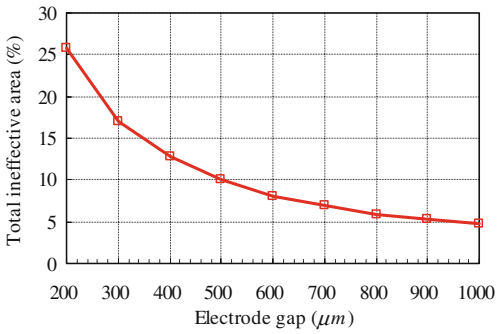

Fig. 6 Tendency of the ineffective area with electrode gap variations

constrained to a maximum value, says 400 μm, according to the working range of the on-board power supplier. With limitations in current fabrication process, the width of patterned electrodes (w) and the gaps (g) between them could not be smaller than 5 μm.

The design variables including electrode width (w), gap between electrodes (g) and the applied voltage (V) in poling process are varied and are automatically updated for each iteration following the subspace approximation and first order algorithm in ANSYS® software [26]. By tracking the variation of design variables and objective function we can monitor how the poling process is affected by electrode width, gap between electrodes and applied voltage. The analysis is terminated when the difference in objective function of two successive iterations is smaller than some given tolerance.

4 Results and discussions

4.1 Effects of the electrode gap and width

It has already been shown that "*dead zones*" exist below the electrode fingers, with the field magnitude being low, and out of plane [16, 17]. With larger electrode separation the proportion of dead zones is lower. Meanwhile, the voltage required to operate the device is higher. In contrast, small electrode separations lower the operational voltage, but increase the proportion of "*dead zones*". There should be a compromise between the achievable actuation strain and operational voltage. Figure 6 shows a typical tendency of the ineffective area in RVE of an electrode design with electrode gap variations and other fixed parameters. Moreover, for thinner substrates the electrode separation can be reduced significantly while still maintaining a high proportion of the optimum d_{33}-mode response.

It was found that by increasing the electrode width the electric field strength in the x-direction between electrodes is increased and the "*dead zone*" under the electrodes, where the field in the x-direction is relatively low, also becomes larger [16]. The electric field in the "*dead zones*" is perpendicular to the actuation direction (x). For thinner electrodes, a relatively weak field is observed between the electrode fingers. It was reported that there exists an optimum width of electrode for which the strain per unit applied voltage is at a maximum, and this optimum width is independent of electrode separation and wafer thickness [17]. The poling study has showed that a field concentration exists at the electrode edges [20]. The magnitude of the field strength in this location increases as the electrode width is reduced, whilst the direction remains largely unaffected. The non-uniform fields present at electrode edges can cause cracking of the piezoelectric substrate resulting in device deterioration. This is a consequence of the large and non-uniform mechanical stresses induced via the piezoelectric effect. Although induced stresses are not quantified in this study, they can be an important effect that leads to device failure.

4.2 Optimization of the active layer with surface IDEs

For comparing purpose, the thickness of the PZT wafer is chosen the same as in the original LIPCA. Moreover, from previous argument, one can see that with the larger gap between electrodes, the higher strain can be generated. However, with a large gap, the operating voltage will be increased. As explained above, the chosen gap is a compromise between achievable actuation strain and operational voltage. It is then constrained to a maximum value of 400 μm in the d_{33}-mode LIPCA hereinafter. The optimum poling process is achieved with the optimum set of design variables given in Table 4. The electrode width w=133 μm, gap between electrodes g=400 μm and the applied voltage V=1358 V_{pp}.

Table 4 Optimal design for a typical active layer with surface IDEs

Electrode width w (μm)	133
Electrode spacing$g$ (μm)	400
Applied poling voltage (V)	1358 V_{pp}
Portion of breakdown volume	0.998%
Portion of unpoled volume	19.27%
Total ineffective volume portion	20.27%

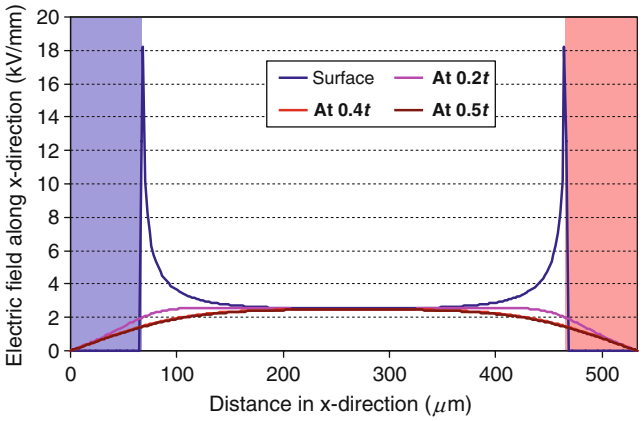

Fig. 7 Longitudinal component of electric field distribution

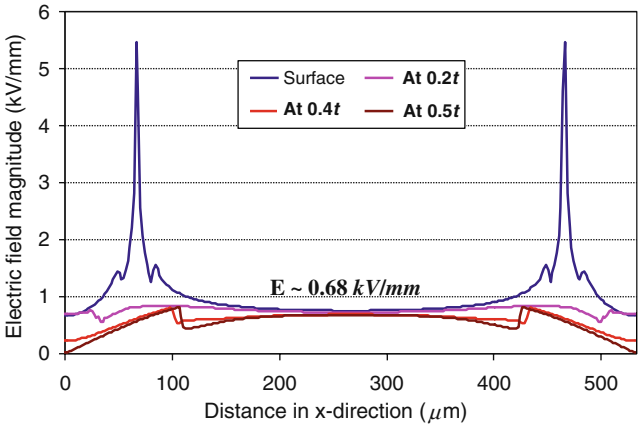

Fig. 9 Electric field distribution due to excitation input

The reduction of actuation is defined as the ratio of the sum of unpoled and high field volume to the total volume.

At optimized condition, a reduction of about 20.3% volume is obtained. That means, almost 80% volume of the PZT wafer contribute to the d_{33}-mode actuation of the new LIPCA. Roughly, with the same applied electric field, the new design could give an improvement of about 72% in curvature change following the analysis in Table 2. The distributions of electric field on the surfaces and inside the ceramic wafer (at 20%, 40% and 50% of thickness below the surface) are given in Figs. 7 and 8.

The design is then verified by applying a ±200 V signal to compare the actuation with the d_{31}-mode counterpart. The obtained picture of electric field distribution on the surfaces and inside the RVE is given in Fig. 9. The uniform electric field in the effective region can be obtained by the graph of magnitude 0.68 *kV/mm*. Once again, the highly concentrated value can be observed.

To compare the actuation of the d_{31}- and d_{33}-mode PZT wafers, a voltage is applied to generate the same electric field of 0.68 *kV/mm* in the d_{31}-mode PZT wafer. The strain output is recorded and plotted in Fig. 10. Note that, due to the singularity of electric field distribution in neighborhood of the electrode tips, the strain output in this region is fluctuated. This issue is not solved in this study yet. However, the overall actuation is mostly contributed by the uniform electric field region and thus the strain fluctuation of small portions beneath the electrode tips will not affect much the actuator performance. For d_{31}-mode, with the same electric field value, the actuated strain can be generated is: $\varepsilon_{31}=d_{31}E$.

Thus,

$$\varepsilon = 320 \times 10^{-12}(m/V) \times 0.68 \times 10^{6}(V/m) = 217.6\mu\varepsilon \quad (6)$$

The improved strain output for d_{33}-mode PZT wafer with the same applied electric field is shown in Fig. 10. Even in the case d_{31}-mode PZT wafer is opperated at the highest allowed input, that means the electric field in material equals to the *coercive value* E_C, the output strain:

$$\varepsilon_{31,\max} = d_{31} \times E_c = 256\mu\varepsilon < \varepsilon_{33} \quad (7)$$

is still much smaller than the output strain in d_{33}-mode PZT wafer.

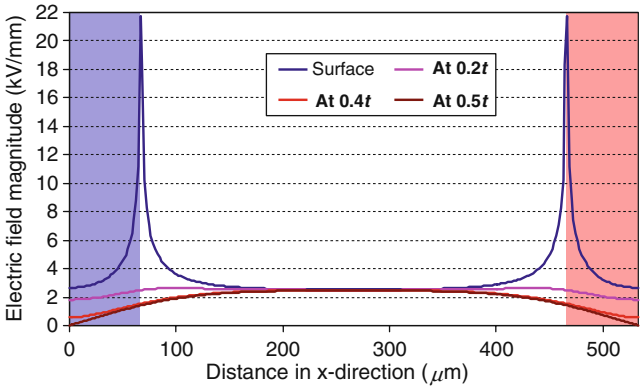

Fig. 8 Distribution and magnitude of electric field

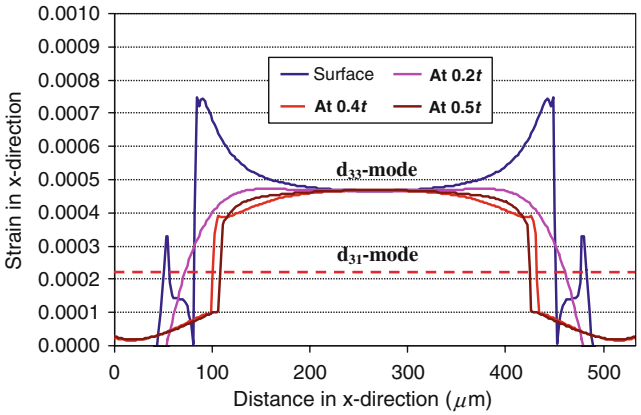

Fig. 10 Comparison of the actuated strain in d_{31}-and d_{33}-mode wafers

5 Conclusion

Attempts to improve the performance of piezoelectric actuator introduced in this study include employ the residual stress effect and exploit the more favorable actuation mode. The former contribution may be conducted by the stress state in the PZT layer whilst the latter utilizes the fact that d_{33} coupling effect is almost double d_{31} effect. The residual stress in piezoelectric material layer due to curing process and applied mechanical load could be a crucial factor in improving the actuation of LIPCA. The proposed state-of-the-art d_{33}-mode LIPCA design in this work aims to utilize the more preferable actuation mechanism to improve the performance. A simple analytical model developed has shown that, with the same applied electric field, LIPCA operated with perfect d_{33}-mode can theoretically generate a curvature change value almost twice of that in case LIPCA operated with d_{31}-mode. However, the d_{33}-mode LIPCA using surface IDEs piezoelectric ceramic wafer as the actuation layer is not associated with a perfect d_{33}-mode actuation mechanism. This is because the in-plane polarized condition of PZT cannot be fulfilled with a poling process using surface IDEs system. The piezoelectricity is thus strongly anisotropic and inhomogeneous throughout the active layer. There exists "*dead zones*" where materials are poled in an out-of-plane direction or still unpoled after the poling process. Such areas lead to a reduction in contribution to the overall actuation of the active wafer. The optimization process helps to minimize these portions and to obtain a maximum effective volume. The new LIPCA with the optimum set of design variables can be improved about 72% of curvature change. However, the portion of high field volume is still high, that could lead to some damage for the actuator. Finding a solution to reduce the high field value as well as the high field volume is the next goal of this research.

Acknowledgment This paper was supported by Konkuk University in 2011.

References

1. A.A. Bent, N.W. Hagood, Piezoelectric fiber composites with interdigitated electrodes. J. Intell. Mater. Syst. Struct. **8**(11), 903–919 (1997)
2. R.G. Bryant, Overview of NASA Langley's Piezoelectric Ceramic Packaging Technology and Applications, NASA Technical Report, NASA Langley Research Center, (2007)
3. K.H. Park, B.S. Yoon, N.T. Nguyen, N.S. Goo, T.S. Kang, K.J. Yoon, Piezo-composite actuated control surface system for flying vehicle. Aircraft Eng. Aero Tech. **82**(6), 372–375 (2010)
4. K.J. Yoon, N.T. Nguyen, Development of piezo-composite actuator LIPCA and its application to biomimetic robots, The Third International Symposium on Aero Aqua Bio-mechanisms (ISABMEC), Ginowan, Okinawa, Japan (2006)
5. K.J. Yoon, K.H. Park, S.K. Lee, N.S. Goo, H.C. Park, Analytical design model for a piezo-composite unimorph actuator and its verification using lightweight piezo-composite curved actuators. Smart Mater. Struct. **13**, 459–467 (2004)
6. N.T. Nguyen, B.S. Yoon, K.J. Yoon, An Improved Design of Piezo-composite Actuator used as the Artificial Muscle for Bio-inspired Robots, IEEE International Conference on Robotics and Biomimetics, Sanya, China (2007)
7. Q.V. Nguyen, H.C. Park, N. S. Goo, Flapping performance of a flapper actuated by the compressed LIPCA, World Forum on Smart Materials and Smart Structures Technology (SMSST '07), Chongqing and Nanjing, China (2007)
8. K.J. Yoon, H. Setiawan, N.T. Nguyen, H.C. Park, Development of Elevator Control Surface for Small Air Robot Using Piezoceramic Actuator, IEEE International Conference on Robotics and Biomimetics (ROBIO), Kunming, China (2006)
9. N.-T. Nguyen, B.-S. Yoon, K.-J. Yoon, Actuation characterization of the lightweight unimorph piezo-composite actuator for different loading cases. Advanced Composite Materials (submitted) (2010)
10. N.T. Nguyen, B.S. Yoon, K.J. Yoon, An experimental study to improve the performance of unimorph piezoelectric actuators subjected to external loading, SPIE's 14th Annual International Symposium on Smart Structures and Materials, San Diego, CA, USA, (2007)
11. N.T. Nguyen, K.J. Yoon, H.C. Park, Actuation displacement of unimorph piezoelectric actuators with external loading. J. Korean Phys. Soc. (2006)
12. N.-T. Nguyen, J.-H. Kweon, K.-J. Yoon, Design analysis of a 3–3 mode piezocomposite actuator. Advanced Composite Materials (accepted) (2010)
13. K.J. Yoon, Y.S. Yoon, H.C. Park, N.S. Goo, Electro Active Material Actuator Embedded with Interdigitated Electrodes, International App. No. PCT/KR2005/003417 (2005)
14. W.K. Wilkie, R.G. Bryant, J.W. High, R.L. Fox, R.F. Hellbaum, J. A. Jalink, B.D. Little, P.H. Mirick, Low-cost piezocomposite actuator for structural control applications, SPIE's 7th Annual International Symposium on Smart Structures and Materials, Newport Beach, CA (2000)
15. W. Wilkie, W. Williams, J. High, D. Inman, *Recent Developments in NASA Piezocomposite Actuator Technology, Actuator 2004: 9th International Conf. on New Actuators, Paper A 4.9* (2004)
16. W. Beckert, W.S. Kreher, Modelling piezoelectric modules with interdigitated electrode structures. Comput. Mater. Sci. **26**, 36–45 (2003)
17. C.R. Bowen, L.J. Nelson, R. Stevens, M.G. Cain, M. Stewart, Optimisation of interdigitated electrodes for piezoelectric actuators and active fibre composites. J. Electroceram. **16**(4), 263–269 (2006)
18. R. Paradies, M. Melnykowycz, Numerical stress investigation for piezoelectric elements with a circular cross section and interdigitated electrodes. J. Intell. Mater. Syst. Struct. **18**, 963–972 (2007)
19. R.J. Werlink, R.G. Bryant, D. Manos, *Macro fiber piezocomposite actuator poling study, NASA/TM-2002-211434* (NASA Langley Research Center, Hampton, Virginia, 2002)
20. N.-T. Nguyen, B.-S. Yoon, K.-J. Yoon, Simulation of the poling process for Macro-Fiber Composite (MFC) actuator. Sensors and Actuators A: Physical (to submit)
21. G. Stranford, *Personal Communication*. (CTS Wireless Inc., 2007)

22. S.C. Hwang, J.E. Huber, R.M. McMeeking, N.A. Fleck, The simulation of switching in polycrystalline ferroelectric ceramics. J. Appl. Phys. **84**(3), 1530–1540 (1998)
23. S.C. Hwang, C.S. Lynch, R.M. McMeeking, Ferroelectric/ferroelastic interactions and a polarization switching model. Acta Metall. Mater. **43**(5), 2073–2084 (1995)
24. S.C. Hwang, R.M. McMeeking, A finite element model of ferroelastic polycrystals. Int. J. Solids Struct. **36**(10), 1541–1556 (1999)
25. A. Messac, A.A. Mullur, Multiobjective optimization: Concepts and methods, in *Optimization of structural and mechanical systems*, ed. by J.S. Arora (World Scientific, Singapore, 2007)
26. http://www.ansys.com/, ANSYS Documentation Manuals